Direct detection of polystyrene equivalent nanoparticles with a diameter of 21 nm (~λ/19) using coherent Fourier scatterometry

Kolenov, D.; Zadeh, I. E.; Horsten, R. C.; Pereira, S. F.

DOI
10.1364/OE.421145

Publication date
2021

Document Version
Final published version

Published in
Optics Express

Research Article | Vol. 29, No. 11 / 24 May 2021 / Optics Express 16487
Optics EXPRESS

Direct detection of polystyrene equivalent nanoparticles with a diameter of 21 nm ($\sim\lambda/19$) using coherent Fourier scatterometry

D. KOLENOV,* I. E. ZADEH, R. C. HORSTEN, AND S. F. PEREIRA

Optics Research Group, Imaging Physics Department, Faculty of Applied Sciences, Delft University of Technology, Lorentzweg 1, 2628 CJ Delft, The Netherlands
*d.kolenov@tudelft.nl

Abstract: Coherent Fourier scatterometry (CFS) has been introduced to fulfil the need for noninvasive and sensitive inspection of subwavelength nanoparticles in the far field. The technique is based on detecting the scattering of coherent light when it is focused on isolated nanoparticles. In the present work, we describe the results of an experimental study aimed at establishing the actual detection limits of the technique, namely the smallest particle that could be detected with our system. The assessment for particles with a diameter smaller than 40 nm is carried out using calibrated nano-pillars of photoresist on silicon wafers that have been fabricated with e-beam lithography. We demonstrate the detection of polystyrene equivalent nanoparticles of diameter of 21 nm with a signal-to-noise ratio of 4 dB using the illuminating wavelength of 405 nm.

1. Introduction

Large scale integrated circuits [1,2], neuromorphic computing [3], bio-sensing monitoring [4], optical networks [5] and optical image processing [6] require the fabrication and associated metrology to be done at the nanoscale. Among other parameters, overlay and contamination control are essential for the semiconductor industry [7]. Lithography devices and surface analysis tools should comply both with the projection of Moore's law [8] and economy [9].

Some years ago, coherent Fourier Scatterometry (CFS) had been suggested as a metrology technique for high-accuracy retrieval of shape parameters of periodic gratings [10,11]. Later on, CFS has also been applied for nanoparticle detection at the visible spectrum range in bright field configuration [12]. The detection is based on focusing a coherent light beam onto the surface that is laterally scanned in 2D. The field that is reflected from the surface is collected by the same focusing lens and directed to a split photodetector, where a differential photocurrent value is obtained point per point of the scan. This scheme allows the use of low power lasers (as compared to darkfield techniques) and is suitable for detection of low optical contrast subwavelength nanoparticles. Besides, one can determine the position of the particles with high accuracy as well as classify their sizes. For the latter, we compare the measured differential scattering signal with a library of calibrated particles. In order to push the detection of nanoparticles from size node of $<\lambda/4$ to $<\lambda/10$ sphere diameter, using a wavelength of $\lambda = 405$ nm, multiple improvement steps have been realised, such as suppression of the experimental noise with heterodyne detection technique [13], accurate focus positioning [14], as well as development of machine learning techniques to locate and extract the relevant features of the particles [15,16].

The most fundamental limitation of the CFS technique is the signal-to-noise ratio (SNR) at the detector, where the most stringent contribution to the detector signal comes from the nanoparticle since it is well known from the Rayleigh theory that the scattering cross-section decreases considerably with decreasing of the particle volume [17]. In addition, technical noise from the electronics and environmental noise such as vibrations cannot be completely eliminated. To date,

#421145 https://doi.org/10.1364/OE.421145
Journal © 2021 Received 28 Jan 2021; revised 1 Apr 2021; accepted 25 Apr 2021; published 13 May 2021

Optics EXPRESS

one of the main questions about the application of the CFS technique for particle detection is its sensitivity to the smallest particle size that could be detected with the latest prototype that has been implemented by the authors [13].

In this paper, we perform a theoretical and experimental analysis of the detection limits of the CFS setup. Two types of samples mimicking contamination have been fabricated: for particle diameters above 40 nm, polystyrene latex (PSL) nanoparticles have been spin-coated on a silicon wafer, and for particles with diameters < 40 nm, we have fabricated nano-pillars of resist (Hydrogen silsesquioxane HSQ, representing SiO2) with corresponding Latex Sphere Equivalent (LSE) sizes down to a diameter of 21 nm. This paper presents, for the first time, the detection of low contrast nanoparticles with diameter of 21 nm with a signal-to-noise ratio $SNR \approx 4$ dB at a wavelength of 405 nm ($\sim \lambda/19$) using CFS. Achieving far field detection of extremely low contrast nanoparticles in the deep subwavelength regime at a low power level paves the way for proof-of-concept experiments in areas such as inspection of plastic and glass substrates for nanoimprinting and roll-to-roll applications, as well as in biological samples for label-free detection and classification of bio-nanoparticles and contamination due to viruses and bacteria.

The remainder of the paper is organized as follows: Section 2 is devoted to the description of the optical system, analytical modelling of a dipole, and definition of metrics to estimate the scattering from non-spherical particles. In Section 3.1, we show the experimental results of nanoparticle detection. Further, in Section 3.2, we present the numerical and experimental analysis of surface roughness of the substrate. In Section 3.3, we combine the different measurement factors to explain the limits of nanoparticle detection. We finalize the paper with conclusions in Section 4, followed by the appendices.

2. Methods

2.1. Experimental setup

The setup of the CFS for nanoparticle detection is shown in Fig. 1(A). A linealy polarized collimated diode laser at 405 nm (Power Technology, model: IQ1A25), is reflected by the beam splitter cube towards a $NA = 0.9$ objective, where the light is focused at the interface between air and a silicon wafer. The 2D lateral raster scanning xy of the wafer is performed with a piezo translator (P-629.2CD by Physik Instrumente) with a z-translator on top for accurate focusing positioning (P-620.ZCD). The scattered and reflected light passes through the same objective and is directed to the split detector (ODD-3W-2 Bi-Cell Silicon Photodiode), where the far field, corresponding to the exit pupil of the objective, is imaged. Heterodyne detection is implemented by modulating the laser and using a lock-in amplifier (MFLI 500 KHz, Zurich Instruments). We use sufficiently high modulation and referencing with the sinusoidal waveform of $f_m = f_r = 30$ kHz. In Fig. 1(B) we show the far-field intensity distributions (obtained with rigorous 3D electromagnetic simulations [18]) that correspond to significant particle positions in scanning - Fig. 1(C). The particle being scanned in the x-direction through the focused spot for 3 positions of the particle centre, namely to the left, centred, and to the right of the focused spot. The y-axis is centred with respect to the particle in this case. The split detector is placed at the far-field plane and the two halves (left and right) are integrated and subtracted from each other such that a photocurrent value for each X position of the scan is obtained. The resulting differential signal, when the particle is scanned under the focused spot is shown in the inset. N.B. The peak-to-peak amplitude V_{pp} of the differential signal is the crucial parameter that will be used to determine the particle size.

Optics EXPRESS

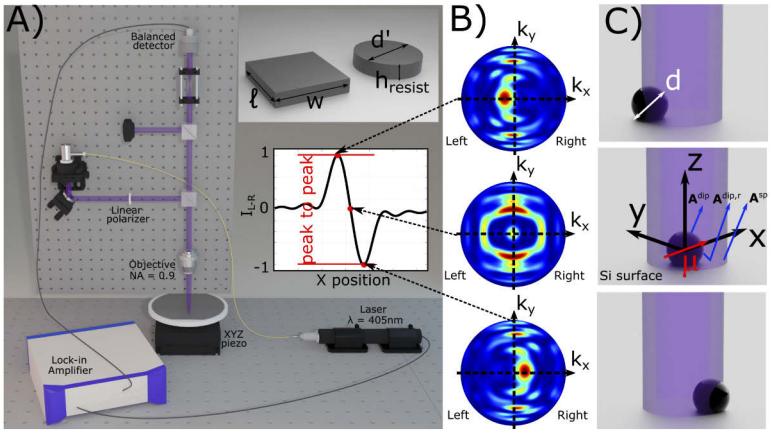

Fig. 1. A) 3D illustration of the CFS for nanoparticle detection setup. In the upper inset, we see the drawing of the square prism and cylindrical shape nanoparticle made of resist. In the lower inset, we see normalized differential signal I_{L-R} (Left minus Right) obtained from simulation when the particle is scanned under the focused spot in the x-direction. B) Simulated far field intensity distribution at the balanced detector for three positions of the particle with respect to the focussed spot. C) Scheme showing 3 positions in the x-direction of the substrate containing one particle under the focused spot with the nanoparticle on the left, centered, and on the right of the spot. The particle is centered with respect to the y-direction. Middle image - the analytical modeling of the problem showing the far-field contributions: directly scattered, reflected scattered and specular reflected field $\mathbf{A}^{out} = \mathbf{A}^{dip} + \mathbf{A}^{dip,r} + \mathbf{A}^{sp}$.

2.2. Model of the particle-field interaction

The scattering of light that illuminates a sphere located at an interface consists of three contributions: 1) free-space dipole radiation, 2) light scattered from the dipole to the interface and further reflected to the far field, and 3) specular reflection from the interface (see scheme in Fig. 1(C), center). Let us consider a Cartesian system (x, y, z) with the z as propagation direction. Following the formalism outlined in Ref. [19], an electric dipole in air with a dipole vector $\boldsymbol{\mu} = (\mu_x, \mu_y, \mu_z)$ is placed at the origin. If an objective, with the z axis as the optical axis, is placed such that its geometrical focus is at the origin, then the outgoing perpendicular (s) and parallel (p) fields (unit vectors of $\mathbf{s}$ and $\mathbf{p}$) of the particle in air can be described as $\boldsymbol{A}^{dip}$:

$$\boldsymbol{A}^{dip} = A_s^{dip}\mathbf{s} + A_p^{dip}\mathbf{p} \tag{1}$$

$$A_s^{dip} = \frac{1}{2i\epsilon_0}\frac{k/k_z}{\sqrt{k_x^2 + k_y^2}}\left[kk_x\mu_y - kk_y\mu_x\right] \tag{2}$$

$$A_p^{dip} = \frac{1}{2i\epsilon_0}\frac{k/k_z}{\sqrt{k_x^2 + k_y^2}}\left[k_xk_z\mu_x + k_yk_z\mu_y - (k_x^2 + k_y^2)\mu_z\right]. \tag{3}$$

It is also known that the field at the focus of a linearly polarized light beam at the pupil has a large transversal component [20]. If the dipole moment is oriented along x, i.e., $\mu_y = \mu_z = 0$, then the electric field in the pupil has both contributions of s and p polarized light given by:

$$A_s^{dip} = -\frac{\mu_x}{2i\epsilon_0}\frac{k^2k_y}{k_z\sqrt{k_x^2 + k_y^2}} \tag{4a}$$

Optics EXPRESS

$$A_p^{dip} = \frac{\mu_x}{2i\epsilon_0}\frac{kk_x}{\sqrt{k_x^2+k_y^2}}. \tag{4b}$$

A reasonable approximation of the dipole moment $\boldsymbol{\mu}$ is to assume it to be proportional to the incident local electric field $\boldsymbol{E}^f$ at the position of the nanoparticle through the complex polarizability α:

$$\boldsymbol{\mu} = \alpha \boldsymbol{E}^f, \tag{5}$$

where the parameter α depends on the material permitivity ϵ, diameter d of the nanoparticle, and the permitivity of the surrounding medium ϵ_m:

$$\alpha = 4\pi\epsilon_m\left(\frac{d}{2}\right)^3\frac{\epsilon-\epsilon_m}{\epsilon+2\epsilon_m}. \tag{6}$$

If the incident field is x-linearly polarized before the objective, then close to the focus and around the optical axis $\boldsymbol{E}^f(\mathbf{r}) \approx E^f(\mathbf{x})\hat{z}$. Following the shift properties of the Fourier transform, if we shift the nanoparticle in the focal plane along the x-axis by $r = X$, then there will be a corresponding phase shift of ik_xX in the scattered far field.

$$A_s^{dip} = -\frac{\alpha}{2i\epsilon_0}\left[\frac{k^2k_y}{k_z\sqrt{k_x^2+k_y^2}}\right]E^f(x)e^{ik_xX} \tag{7a}$$

$$A_p^{dip} = \frac{\alpha}{2i\epsilon_0}\left[\frac{kk_x}{\sqrt{k_x^2+k_y^2}}\right]E^f(x)e^{ik_xX}. \tag{7b}$$

Eqs. (7a) and (7b) represents the amplitudes of the field directly scattered from the dipole to the pupil plane $\boldsymbol{A}^{dip}$. Further, to take into account the interaction of the dipole and the surface, we assume that the dipole is very close to the interface so that the phase difference between the directly scattered and reflected scattered signal is very small. This assumption is approximately valid when the beam is focused at the interface, so that the effective dipole remains very close to the surface. Moreover, this phase is not a function of x. Thus, the total scattered signal $\mathbf{A}^{dip} + \mathbf{A}^{dip,r}$ can be obtained by multiplying Eq. (7a) by $1 + r_s$ and Eq. (7b) by $1 + r_p$ where, r_s and r_p are the complex Fresnel reflection coefficients for s and p polarization, respectively and they represent the air/silicon interface.

Lastly, the pupil plane will have the contribution of the spurious reflected field from the interface (incident field $\mathbf{A}^{inc}$ modulated by Fresnel coefficients), given by the specular reflected fields:

$$\boldsymbol{A}_s^{sp} = r_sA_s^{inc}\boldsymbol{s} \tag{8a}$$

$$\boldsymbol{A}_p^{sp} = r_pA_p^{inc}\boldsymbol{p}. \tag{8b}$$

Thus, the total outgoing complex field $\boldsymbol{A}^{out}$ can be written as a superposition of a spurious reflected and a total scattered wave as:

$$A_s^{out} \approx r_sA_s^{inc} - (1+r_s)\frac{\alpha}{2i\epsilon_0}\left[\frac{k^2k_y}{k_z\sqrt{k_x^2+k_y^2}}\right]E^f(x)e^{ik_xX} \tag{9}$$

$$A_p^{out} \approx r_pA_p^{inc} + (1+r_p)\frac{\alpha}{2i\epsilon_0}\left[\frac{kk_x}{\sqrt{k_x^2+k_y^2}}\right]E^f(x)e^{ik_xX}. \tag{10}$$

The field at the focal region for high numerical aperture systems was firstly formulated by Ignatowsky [21] and re-derived by Richards and Wolf [22]. In this paper, we will rely on the

Optics EXPRESS

derivation from [23] to write down the field in the focal region after passing through a high numerical aperture (NA) imaging system by the x-polarized beam given by:

$$\overrightarrow{E}(\tilde{r},\tilde{\phi}) = -\frac{ik}{2}\left[\left(G_0 + G_2\cos(2\tilde{\phi})\right)\hat{e}_x + G_2\sin(2\tilde{\phi})\hat{e}_y - 2iG_1\cos\tilde{\phi}\hat{e}_z\right], \tag{11}$$

where $\tilde{r}, \tilde{\phi}$ are the spherical coordinates centered at the Gaussian focus with the third coordinate $\tilde{\theta} = \frac{\pi}{2}$ taking into account only the field at the focus plane. The introduced integrals for G_0, G_1, G_2 with the J Bessel function of order n are defined as:

$$G_0 = \int_0^{\theta_1} A(\alpha)\sin\alpha(1+\cos\alpha)J_0(k\tilde{r}\sin\alpha)d\alpha \tag{12}$$

$$G_1 = \int_0^{\theta_1} A(\alpha)(\sin^2\alpha)J_1(k\tilde{r}\sin\alpha)d\alpha \tag{13}$$

$$G_2 = \int_0^{\theta_1} A(\alpha)\sin\alpha(1-\cos\alpha)J_2(k\tilde{r}\sin\alpha)d\alpha. \tag{14}$$

The range of integration is defined by the NA of the objective and the marginal rays travelling through the objective at a focus with angle $\theta_1 = \sin^{-1}(NA)$. These integrals have no known analytical solution but can be evaluated numerically. Accordingly, the electric field in focus is solved by calculating Eq. (11), with the aid of Eqs. (12), (13) and (14). The E_x and E_z components of the electric field in the focal plane have a much larger absolute value than the remaining E_y part. Accordingly, the combination of these two components will render the highest contribution to the field scattered from the particle to the pupil.

For the profile of the field oriented in the x-direction (the axis of our scanning), the Y should be set to zero. Accordingly, the second term in Eq. (11) vanishes. For all k_x and k_y limited by the NA of the system, the intensity at the pupil is given by:

$$I^{pupil} = |A_s^{out}|^2 + |A_p^{out}|^2. \tag{15}$$

Further integrating and subtracting the two halves of the far field renders the signal of the particle:

$$I_{L-R} = \iint_L I^{pupil} - \iint_R I^{pupil}, \tag{16}$$

These results are important for the vibration estimation in the system as summarized in Appendix C. Further, the presented scattering due to a particle on a substrate model that is illuminated by a tightly focused beam can also be of interest in other applications such as effects taking place in nanoscopic position sensing [24] or characterisation of bio-particles from light scattering [25].

Polystyrene particles $n_{PSL} = 1.57$ ($\lambda = 405$ nm) are standard for the calibration of surface inspection tools because they have well-characterized optical properties (low index of refraction, thus most challenging to detect) [26]. When analyzing resist particles in our case, with even a lower refractive index $n_{resist} = 1.45$, the scattered cross-sections are converted to the Latex Sphere Equivalent (LSE). From the Rayleigh scattering cross-section [27]:

$$\sigma_s \propto \frac{d^6}{\lambda^4}\left(\frac{m^2-1}{m^2+2}\right)^2, \tag{17}$$

where σ_s represents the amount of scattering, d is the diameter of a sphere, m depends on particle material, being equal to $m = \sqrt{n^2+k^2}$ (n and k is a real and imaginary part of refractive index

Optics EXPRESS

respectively). The Hydrogen silsesquioxane (HSQ) particles are either square prisms or cylinders, and using the formulas for their volumes, we can deduce the equivalent sphere diameter:

$$\frac{1}{6}\pi d^3 = wlh_{resist} = \frac{\pi}{4} d^{'} h_{resist} \tag{18}$$

$$d_{sphere-equiv} = \left(\frac{6}{\pi} wlh_{resist}\right)^{\frac{1}{3}} = \left(\frac{3}{2} d^{'} h_{resist}\right)^{\frac{1}{3}}, \tag{19}$$

where w and l are the width and the length of the resulting rectangular prism ($w = l$ for our fabricated structure), $d^{'}$ and h_{resist} are the diameter of cylindrical particle and the height of the resist. Finally, omitting power dependence, we compute the Latex Sphere scattering Equivalent:

$$LSE \approx d_{sphere-equiv} \times \left(\frac{(m^2_{resist} - 1)(m^2_{psl} + 2)}{(m^2_{resist} + 2)(m^2_{psl} - 1)}\right)^2. \tag{20}$$

For materials and the estimates for the LSE see Appendix A.

3. Results

The contamination/defect inspection aims to detect a wide range of particles. The losses in the fabrication yield are estimated based on the location, number, and size composition of the contamination on the inspected surface. In this regard, the traceability of the results is crucial, meaning that a comparison should be made between the tool that is being validated and a reference instrument. A rigorous way to validate the results is to check the same region of interest on the wafer with a reference instrument. This can not be done unless unique surface markers are introduced. In Section 3.1, we present the experimental results of the fabricated samples with markers containing nanoparticles made of resist. In Section 3.2, the reflectance from a rough silicon substrate is numerically analyzed using 3D FEM, combined with roughness measured with an AFM (Appendix A) for both spin-coated samples and the developed silicon surface of the e-beam lithography (EBL) sample. With that, we provide a figure of merit for the roughness background level estimates (Section 3.3), where we include the electronic noise from the detector circuit (Appendix B) and analyse the influence of environmental vibration (Appendix C) using the experimental particle signal calibration curve and fitted power law.

3.1. Experimental results on the minimum size limit of particle detection

As discussed above, in order to be sure about the detection and localization of all individual particles, one would like to compare the scanned area with the corresponding image obtained by a high-resolution imaging technique, such as scanning electron microscope (SEM). To address the issue of producing low-index $<\lambda/10$ particles with a mean separation of ≥ 1 μm, we have fabricated resist nanoparticles on silicon wafers using EBL. We used negative resist samples made with EBL because it allows for the precise control of the particle size as well as the separation between the isolated nanoparticles. We write the enclosed reference structure and the particle array of tiny pillars with two spot sizes to improve upon the writing speed. After the surface scan of the reference structure with CFS is performed, the sample is analyzed with a SEM, to provide the comparison. The array of 4×4 resist particles on top the silicon wafer is shown in SEM image (Fig. 2). The size of the manufactured array is a compromise between the time it takes to fabricate/analyze the sample and the number of available target-size particles. Depending on the magnification of the SEM, it is easy to locate the rectangular edge structure Fig. 2(A) or the star marker C). Performing ellipsometric measurements before developing the resist, we measured the height of the resist giving as result $h_{resist} = 25$ nm. Figs. 2(E) and (F) show the SEM images of the isolated resist nanoparticles with either square prism or cylindrical shapes. The LSE of these

Optics EXPRESS

particles are 33 and 30.4 nm for nominal 50 nm square prisms and cylinders, respectively. The resulting differential signal maps obtained with CFS show that all particles within the reference region have been detected (Fig. 2(B) and (G)). The $SNR \approx 16$ dB is sufficiently high to localize all 16 particles.

In estimation $SNR = 10\log_{10}\left(\frac{S}{N}\right)$, where S and N are the signal and noise power respectively. The noise level is computed based on a differential signal of no particle region scanning.

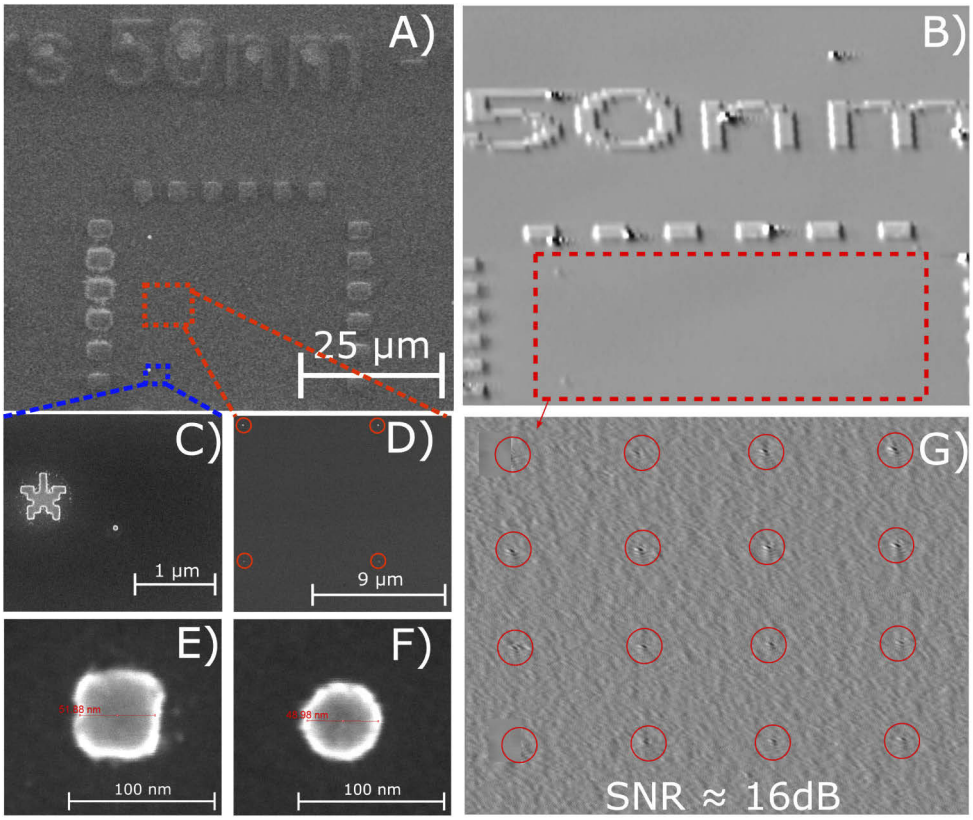

Fig. 2. A) Scanning electron microscope (SEM) image of the reference structure. B) CFS scattered map of the reference region with the close-up G) of all 16 particles that have been detected in a single scan of 34.6×37 μm. C) SEM image of the star (marker) of ≈ 700 nm next to the 50 nm cylinder. D) The nanoparticles separated by 9 μm with the square prisms and cylinders in the upper and bottom rows. E) and F) SEM images of the 50 nm square and cylinder respectively.

In order to check the ability of the CFS system to detect smaller particles, we fabricated another sample containing guiding lines of 4×0.5 μm and 25 nm resist cubes. The lines made of resist facilitate the localization of the nanoparticles both with SEM and CFS. Figure 3(A) displays the measurement with CFS where the three cube nanoparticles have been detected. The exact size of these nanoparticles is confirmed with the SEM image shown in Fig. 3(B). With this measurement, we validate the detection of nanoparticles of diameter $LSE \approx 21$ nm (resist cube of $25 \times 25 \times 25$ nm). For an incident power level of $P \approx 20$ μW, a $SNR \approx 4$ dB has been obtained. We remind that the wavelength used in these measurements was $\lambda = 405$ nm. For the fabrication of the samples see Appendix A.

Optics EXPRESS

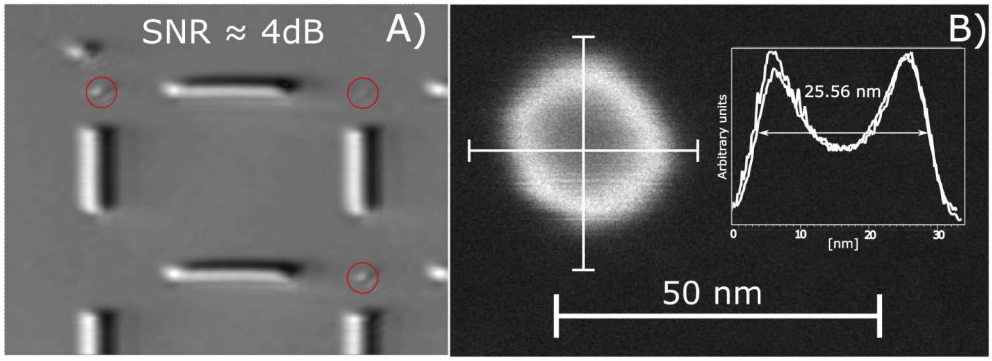

Fig. 3. A) CFS scattered map of the reference region where the three cube nanoparticles are visible ($17.2 \times 17.2\ \mu m$). B) Scanning electron microscope (SEM) image of the ≈ 25 nm cube nanoparticle. In the inset, we see the cross-sections of the particle image in two orthogonal directions

3.2. *Effects of the roughness of the surface*

The differential detection mode is sensitive to irregularities in reflection from the surface of the substrate. These irregularities can come in the form of, e.g. surface roughness, contamination or defects around the particles. For the same optical properties of surface and particle (height of the surface roughness reaches the diameter of the particle $h_{RMS} \approx d$) the signal from the particle will be in the order of the of the scattered signal from the surface. For the case of particles or contamination with low refractive index on a high refractive index silicon substrate, the reflectance can be monitored. Compared to the perfectly flat interface, the reflectance will drop if multiple particles or roughness are present.

In order to understand the influence of roughness, we have performed some rigorous simulations. Within the FEM solver [28], two-dimensional rough surfaces can have variations along the lateral directions. The rough surface height profile is based on a centralized Gaussian distribution in space given by:

$$g(x, y) = e^{-\frac{1}{2}(\frac{x}{c_x})^2 - \frac{1}{2}(\frac{y}{c_y})^2}, \tag{21}$$

which is randomly displaced while summed and normalized. This operation can be written in terms of a 2D forward $\mathcal{F}$ and inverse $\mathcal{F}^{-1}$ Fourier transform:

$$h(x, y) = C\mathcal{F}^{-1}\left[\mathcal{F}[g(k_x, k_y)]e^{i\phi(k_x,k_y)}\right], \tag{22}$$

where the scaling factor C is determined such that the

$$h_{RMS} = \lim_{l\to\infty} \frac{\int_{-l}^{l}\int_{-l}^{l} h^2(x, y)dxdy}{\int_{-l}^{l}\int_{-l}^{l} 1dxdy}. \tag{23}$$

The displacement is according to the deterministic pseudo-random number generator that affects the phase function $\phi(k_x, k_y)$. The resulting roughness of the scattering structure is statistical in nature; thus, the average results of the simulations should be considered. The effect of varying one of the surface parameters $L_c = [c_x, c_y]$ (correlation length) with the other being fixed h_{RMS}, and vice-versa is displayed in Fig. 4. The variation of h_{RMS} can be intuitively understood, while the surface correlation describes the statistical independence of two points on the surface and increases with the correlation between two neighbouring points. For a smooth surface $L_c = \infty$.

Further, periodic boundary conditions are necessary for the horizontal directions to account for the scattering out of the sides of the unit cell. Another reason is to mitigate the drawbacks

Optics EXPRESS

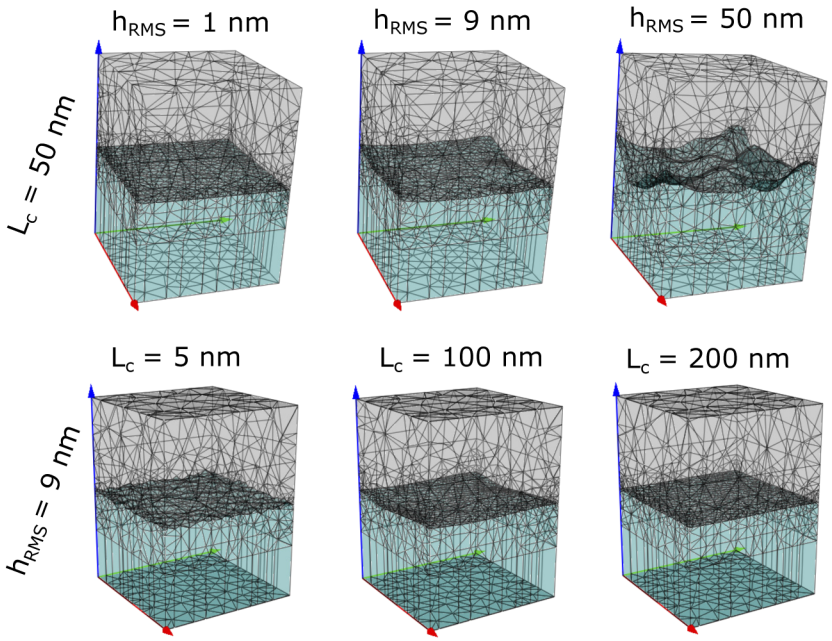

Fig. 4. 3D FEM simulation volume with dimensions of $600 \times 600 \times 800$ nm. The interface between two media is defined as the rough surface with two parameters: height h_{RMS} and correlation length L_c. Fixed $L_c = 50$ nm with varying h_{RMS} in the upper panel, and fixed $h_{RMS} = 9$ nm with varying L_c in the bottom panel.

related to the finite surface size such as the reduction in the angular resolution of scattered fields, as well as the potential influence of scattering and diffraction from the surface edges [29].

We estimate the influence of h_{RMS} on the reflection from the silicon surface assuming an refractive index of $n_{Si} = 5.43 + i * 0.34$ at 405 nm. The rough silicon is normally illuminated by the plane wave with s and p polarization. For periodic cells, as one in Fig. 4, the Fourier transform post-process yields the discrete diffraction modes (amplitudes of the reflected diffraction orders). The amplitudes of the electric plane wave $E(k)\exp(ikx)$ and the magnetic plane wave $H(k)\exp(ikx)$ can be converted to the the power flux density according to $P = \frac{1}{2}\mathbf{E} \times \mathbf{H}^* = \frac{1}{2}\sqrt{\frac{\epsilon}{\mu}}||\mathbf{E}||^2\mathbf{k}^*/||\mathbf{k}||$. Further, the power fluxes in discrete directions of the reflected fields P_r can be divided by the power fluxes of the incoming plane wave P_i to obtain the reflectance $R_s \equiv \frac{P_r^s}{P_i^s}$ and $R_p \equiv \frac{P_r^p}{P_i^p}$. The total reflectance is obtained from the average of both polarizations $R = \frac{R_s + R_p}{2}$.

The real lattice vectors defined for our cell with period $\Lambda = \Lambda_x = \Lambda_y = 600$ nm are $\mathbf{a_1} = [\Lambda, 0, 0]$ and $\mathbf{a_2} = [0, \Lambda, 0]$. The corresponding reciprocal vectors $\mathbf{b_1}$, $\mathbf{b_2}$ are defined such that $b_i \cdot a_j = 2\pi\delta_{ij}$. Hence the reciprocal vectors are $\mathbf{b_1} = [\frac{2\pi}{\Lambda}, 0, 0]$ and $\mathbf{b_2} = [0, \frac{2\pi}{\Lambda}, 0]$, such that $\mathbf{a_1} \cdot \mathbf{b_2} = 0$ and $\mathbf{a_1} \cdot \mathbf{b_1} = 2\pi$. The Fourier modes available for the observation are linked to the reciprocal grid in k-space, where the transversal components of the k-vector in the pupil are defined as $\mathbf{k}_{\perp,n_1,n_2} = n_1\mathbf{b}_{\perp,1} + n_2\mathbf{b}_{\perp,2}$. The remaining normal components k_z are determined by $k_z = \sqrt{k_m^2 - |\mathbf{k}_\perp|}$, where the wave number in the material is given by $k_m = k_0 n_{Si}$ and free-space wavenumber $k_0 = 2\pi/\lambda$. To compute the total number of orders, one needs to determine all the integers n_1, n_2 such that the corresponding k-vectors are propagating $Re\{k_z\}>0$. Alternatively, if the pupil plane is limited by the NA, the following criteria should be satisfied: $Re\{|\mathbf{k}_\perp|/k_0\} \leq NA$. It is evident that only five modes will propagate within the NA (see Fig. 5(A)), such that the following combinations of the n_1, n_2 are possible $\mathbf{n_1} = [-1, 0, 0, 0, 1]$ and $\mathbf{n_2} = [0, -1, 0, 1, 0]$.

Optics EXPRESS

We are not interested in reflectance in the normal direction $R_{normal} = R_{0,0}$ with $n_1 = n_2 = 0$. For the remaining diffraction into the higher orders $R_{scat} = R_{-1,0} + R_{0,-1} + R_{0,1} + R_{1,0}$ with the good alignment of the differential detector one could still expect to get a zero signal. Thus, in our worst-case scenario estimate, small roughness scattering is coming fully to one half of the detector, so we will rely on $R_{scat} = R_{-1,0}$. For the rough surface of $L_c = [50, 50]$ (x and y direction), the parametric sweep of the h_{RMS} from 0.25 to 10 nm, $NA = 0.9$, and $\lambda = 405$ nm as the average result of 400 initializations is shown in Fig. 5(B)). When estimating the peak-to-peak amplitude emerging from the surface roughness, we will rely on the reflectance coefficients of Fig. 5(B)) combined with average roughness height from the AFM. With the growing height of the roughness, the reflectance into the upper half space orthogonal to the surface R_0 decreases. At the same time, the reflectance into the higher angles R_{sca} increases. It is fair to assume that the scattering into the higher angles will define the amplitude of the differential signal. For our optical setup, the power at the detector P_{det} can be estimated as:

$$P_{det} = P_f R_{scat} T_{opt}, \tag{24}$$

where P_f is the power incident on the surface and T_{opt} is the transmission through beamsplitter and other optics; $T_{opt} \approx 0.28$ in our case. Further, taking into account the properties of the detector, the output amplitude is equal to:

$$V_{out} = P_{det} S G, \tag{25}$$

where S is the responsivity of the detector and G is the gain of the differential detector circuit.

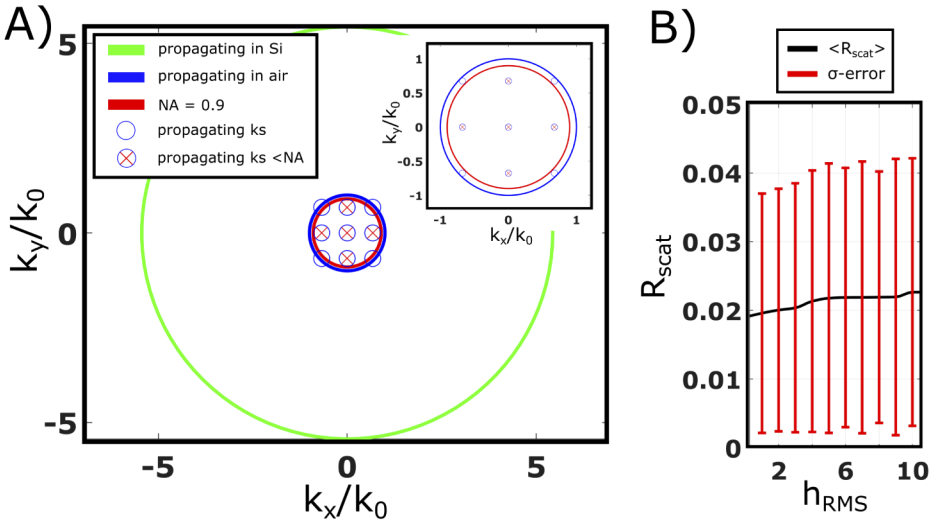

Fig. 5. A) The Fourier space showing the propagating wave vectors for the air/silicon interface at $\lambda = 405$ nm and periodic cell of $\Lambda = 600$ nm. B) The average reflectance coefficient for the non-normal direction within the pupil.

3.3. Limit of detection

In order to establish the smallest LSE diameter particle that can be detected by means of the developed CFS system, we measured two types of samples. The first type are PSL nanospheres that have been spin-coated on 1-inch wafers with a mean separation of ≥ 1 μm between the isolated particles, and the second type are negative-resist square prisms or pillars made with the EBL. A summary of the fabrication and types of samples is presented in Appendix A.

Optics EXPRESS

For each sample, we performed at least four runs (different measurement days) accessing more than three areas on the sample, and analyzed the signal in the time domain with the aid of the search approach, outlined in Ref. [15], resulting in individual amplitude labelling of hundreds of particles. Also, we study areas without particles to provide the background level estimates for the two types of samples. Fig. 6 summarizes the overall analysis. For the detected particles sizes, the blue diamonds indicate the average value of the V_{pp} with a standard deviation shown in grey error bar. Error emerges mostly from the non-uniformity of particle sizes and vibrations in the setup. The solid red line in the plot is the third-power law curve with the best fit based on the error sum of squares criterion. The correction is done by normalizing to unity and multiplying with the maximum value from the experimentally acquired peak-to-peak amplitudes and adding the offset of the shot noise level U_s.

$$U' = \max U_{exp} \frac{U}{|U|} + U_s. \tag{26}$$

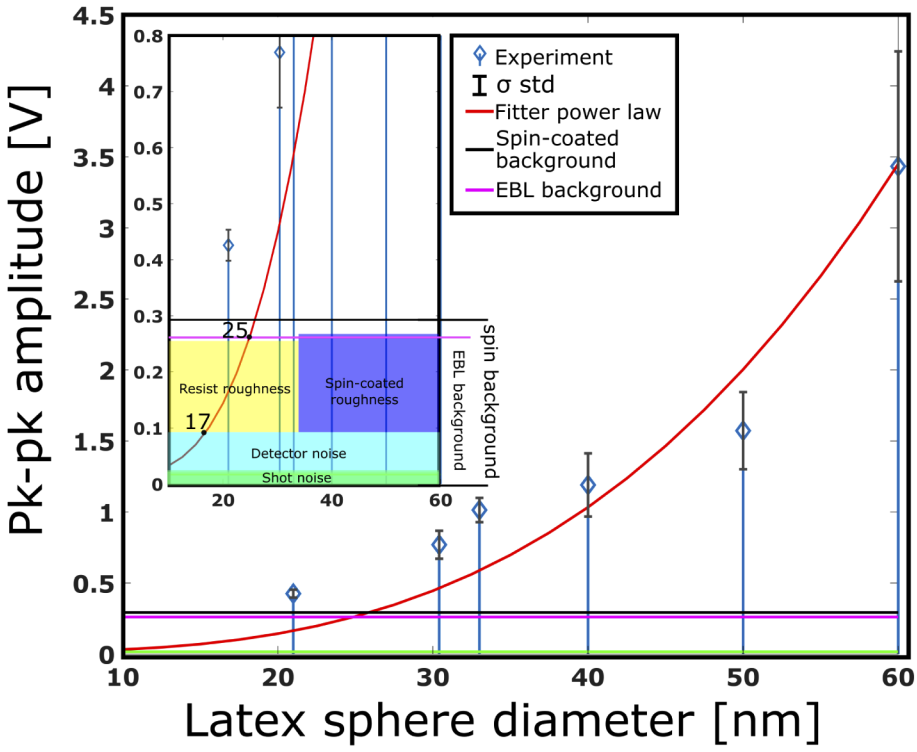

Fig. 6. The peak-to-peak amplitude of the signal (blue diamonds with error bar of σ), fitted power-law (red curve) as function of the latex sphere diameter computed according to Eq. (20). Inset shows experimental background level of the spin-coated particles samples (black line) and samples with particles fabricated with the EBL (magenta line). The background level is further split into the detector noise in light cyan, shot noise in green, and worst-case scenario roughness signal from the EBL-made and spin-coated sample in yellow and purple respectively. Noise and roughness estimation is based on Appendix A and Appendix B.

Further, we include the experimental background levels of the surface signal with no particles for spin-coated and EBL fabricated structures on silicon substrates, represented in the figure by black and magenta horizontal lines, respectively. We colour the amplitude region of the complete detector noise with cyan, shot noise part in green. On top, the estimated *pp* signals from the

Optics EXPRESS

surface roughness of 0.25 nm (in yellow) and of 0.7 nm (in purple) attributed to the developed surface of the EBL sample and spin-residue surface of PSL sample respectively. The crossing between the fitted power curve and the background measured for the EBL sample indicates the smallest detected particle that comes close to experimental one $d_{predEBL} = 25$ nm. Assuming a perfectly flat surface, the intersection between the fitted power law curve and present detector noise is at $d_{pred} = 17$ nm particle. Note that the fact that we obtain a larger pk to pk amplitude than the one expected by the power law suggests that the latter may not be the only contribution to the detected signal, since the combined signals coming from the light scattered by the particle and the one coming from the reflection by the surface may constructively interfere, leading to a stronger signal. In addition, other high order scattering effects and resonances may also occur. This leads to the conclusion that with our present system, even smaller particles could be detected.

4. Conclusions

We have studied the sensitivity limits of the CFS for particle detection. The detection is based on taking a differential signal of a split detector that includes the scattered far field from the nanoparticle plus the reflected light from the substrates, when the latter is illuminated by a focused coherent field. The technique is a scanning technique where for each scan point of the area to be inspected, one value of the split detector signal is recorded.

We conclude that the detection limits of our system are dictated by multiple factors. Firstly, the presence of inherent mechanical noise of the piezo stage (Appendix C). With the current model of the piezo stage, the uncertainty for particle localization in our setup is $\Delta x = 16$ nm. Further, the peak-to-peak fluctuation of the signal indicates the vibration-induced uncertainty of the focal position that is estimated to be $\Delta z = 3$ nm. Accordingly, the design of the setup could be improved to reduce vibrations that couples to the system. For systems requiring faster 2D scan, beam steering combined with 1D piezo scan could be an interesting option.

Next, the investigated electronic noise of the detector is bigger than the one with the Poisson distribution statistics. Based on the analysis of the differential detector circuit (Appendix B), we identify the total noise, including all the noise components using the root sum of the squares. The shunt resistance R_s, junction capacitance C_j of a photodiode, feedback resistance R_f and capacitance C_f of the TIA are the primary parameters used in the noise analysis. In our case, the TIA's feedback resistor noise is the dominant noise source. The theoretical estimate of the resulting noise matches the experimentally measured value for the $E^e_{nout} = 14\ mV_{RMS}$.

Finally, the small scattering cross-section from isolated nanoparticles contributes to the low SNR of the detector signal as the particle diameter decreases. In this work, we demonstrate detection of nanoparticles with 21 nm ($\lambda/19$) LSE diameter, where the main noise sources were due to the combined effect of detector noise and silicon surface roughness $h_{RMS} = 0.25$ nm. We verified the reliability of the CFS bright field scanner by comparing the number of detected scatterers inside the wafer reference region with that of a benchmark SEM measurement. The detection of $LSE \approx 21$ nm particle is achieved with $SNR \approx 4$ dB. This result complies with the requirements for surface inspection in the semiconductor industry (SNR needs to be greater than 3 dB) [30]. The demonstrated detection is promising for initial inspection of a wafer in a fabrication environment, testing a reticle blank, or during the production flow (the pellicle membrane) where non-destructive surface scanning is required. Also, given the compactness of the setup and simplicity of the concept, we believe that such a particle detector could be applied in other areas where surface inspection to this particle size level is required.

Appendix A

In this work, two types of samples were used: spin-coated PSL nanoparticles and negative resist (EBL) deposited on silicon wafers (further called as type 1 and type 2, respectively). Samples

Optics EXPRESS

were prepared in a clean room class ISO 6 and we used high quality 1-inch wafers from Ultrasil. The general procedure for type 1 sample preparation is outlined below:

- Clean UV/Ozone apparatus with isopropyl alcohol (IPA) wipe and switch on for 15 minutes
- Prepare solution
- Place wafer in a beaker in ultrasonic bath
- Clean 1-inch Si wafer in UV Ozone for 5 minute
- Spin 0.5 ml solution on wafer @ 6100 RPM
- Place wafer in box

The solution is prepared by firstly putting 3 droplets of Thermo Scientific nanospheres in 0.5 *ml* demi water (from Merck Simplicity UV water purification system, applied in each recipe), and, secondly, diluting the necessary μl amount in 5 *ml* IPA (Sigma-Aldrich, 2-Propanol, anhydrous, catalogusnummer 278475-1L, applied in each recipe) under vigorous shaking. The summary of solutions made for PSL samples is shown in Table 1.

Table 1. Specification for solute particles and the proportions used

Sample #	Diameter [nm]	Serial number	Amount to delute [μl]
1	100	3100A	80
2	80	3080A	70
3	60	3060A	60
4	50	3050A	50
5	40	3040A	40

In order to fabricate type 2 samples, we followed the procedure of negative resist fabrication:

- The wafer was cleaved to smaller pieces (1×1 or 2×2 *cm*).
- Chips were spun with the HSQ XR-1541 diluted in MIBK resist at different speed to control the thickness.
- E-Beam exposure: 100 kV Raith ebeam lithography system, beam current of 112 pA (estimated spot size of 1.9 nm). The dose is 7250 $\mu C/cm^2$ for the $50 \times 50 \times 25$ *nm* sample and $9500 \mu C/cm^2$ for $25 \times 25 \times 25$ *nm* sample.
- Development: MF322 (1 min) , MF322: $H_2O \sim$ 1:5 (30 sec), H_2O (1 min).

It is crucial to make a dilution of the e-beam resist and perform the spinning at different speed, to optimize for the heights of the future particles. Table 2 summarizes the developed recipes and shows the results of the thickness measured with an ellipsometer (Woollam M5000).

In regions with no particles for the type 1 sample, the average roughness is $h_{RMS} = 0.7$ nm and for the type 2 sample, $h_{RMS} = 0.25$ nm. These measurements were performed with Park NX20 AFM. Given that the refractive indices n are 1.57 (PSL) and 1.45 (resist) at room temperature with a probe wavelength of 405 nm, we estimate the LSEs in Table 3 for the square prism and cylinder resist particles.

Optics EXPRESS

Table 2. HSQ XR-1541 was diluted with MIBK. And spun with different speeds

Recipe #	Dilution HSQ:MIBK (by volume)	Spinning speed (RPM)	Measured thickness [nm]
1	1:2	4000	53
2	1:2	6000	47
3	1:3	6000	25

Table 3. Resit particle types for which the LSE is estimated

Volume of resist particle [nm^3]	Shape of particle	Sphere diam. equiv. [nm]	LSE [nm]
50x50x25	Square Prism	49.23	33
50x25	Cylinder	45.42	30.4
25x25x25	Cube	31.02	21

Appendix B

The circuit of the differential detection (Fig. 7) is optimized for small-signal amplification. The split detector ($ODD-3W-2$) has a common ground that minimizes the pickup of the environmental noise. The photocurrent measured from each diode is converted to a voltage with a trans-impedance amplifier (TIA) with a gain $G_{TIA} \approx 32K$ (Fig. 7(A)). It is advantageous to amplify each photodiode signal separately by having two TIAs instead of subtracting the photodiodes currents, amplifying and converting to voltage. The latter is more susceptible to pickup noise. Further, the subtraction of the two signals and adding additional gain is accomplished by two operational amplifiers. The total gain of this stage is $G_{OPA} \approx 513$ Fig. 7(B)). Accordingly, the complete gain of the circuit is $G \approx 16 \cdot 10^6$. The bandwidth of the circuit is set to $BW = 50$ kHz. Since we perform particle detection in the time domain, it is convenient to express the noise in terms of either peak-to-peak (pp) or RMS values. The figure of merit of V_{rms} should be multiplied by 6.6 to get to the estimate of the peak-to-peak value. The parameters of the SD photodiode are summarized in Table 4.

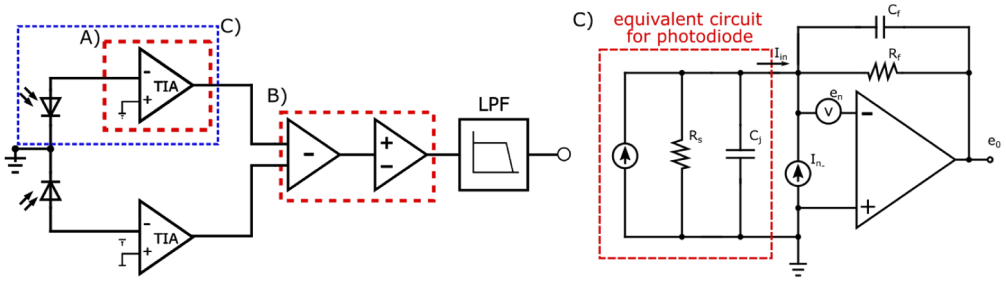

Fig. 7. A) Sketch of the differential detector circuit. The current from each photodiode is converted to voltage by the transimpedance amplifier with a gain $G_{TIA} \approx 32K$. B) The voltages of each TIA are subtracted and amplified with a combined gain of $G_{OPA} \approx 513$. The bandwidth of the circuit is $BW = 50\ kHz$. C) Sketch for modelling of the noise of a single photodiode and TIA circuit. $R_s = 300\ M\Omega$, $C_j = 30\ pF$, $C_f = 33\ pF$, $R_f = 100\ K\Omega$.

We start by computing the shot I_s and Johnson noise I_j of the photodiode:

$$I_s = \sqrt{2q(I_p + I_d)BW}, \tag{27}$$

Optics EXPRESS

Table 4. Parameters of the split detector(s): ODD-3W-2 Bi-Cell Silicon Photodiode

Active area	$2 \times 3.1\ mm^2$
Dark Current	0.9 nA
Responsivity	0.36 (633nm) and 0.1 (405nm)
Noise Equivalent Power	$2.5 \times 10^{-14}\ W/\sqrt{Hz}$
Response time	$\approx$ 190 ns

where q is the electron charge, I_p the photocurrent, I_d the dark photocurrent, and BW the bandwidth.

$$I_j = \sqrt{\frac{4k_BTBW}{R_s}}, \tag{28}$$

where k_B is the Boltzmann constant, T the temperature in Kelvin (estimated for temperature 25°), R_s is the Shunt resistor of photodiode.

The total noise at the photodiode is given by:

$$I_{tp} = \sqrt{I_s^2 + I_j^2}, \tag{29}$$

and the associated voltage noise at the output of TIA can be written as:

$$E_{np} = I_{tp}G_{TIA}. \tag{30}$$

It is a convention to compute the RMS noise of the field-effect transistor (FET) TIA (Fig. 3(C)) using a piece-wise approach [31]. The voltage noise is computed for the low, medium and high frequency region, and the coefficients for the voltage noise density $K_1 = 7$, $K_2 = 3.3$ and $K_3 = 2.1\ nV/\sqrt{Hz}$ are taken from the data sheet for the TIA (ADA4625-1). In the first region, from $f_1 = 0.01$ Hz to $f_c = 100$ Hz

$$E_{n1} = K_1\left[1 + \frac{R_f}{R_s}\right]\sqrt{\ln\left(\frac{f_c}{f_1}\right)}, \tag{31}$$

in the second region, from f_c to $f_a = 1$ kHz

$$E_{n2} = K_2K_3\sqrt{\frac{f_c^3}{3} - \frac{f_a^3}{3}}, \tag{32}$$

and the third region from f_a to $f_3 = 50$ kHz

$$E_{n3} = K_2\left(1 + \frac{C_j}{C_f}\sqrt{\left(\frac{\pi}{2}\right)f_3 - f_a}\right). \tag{33}$$

The output voltage component due to the current noise, with the corresponding coefficient for the current noise density $K_4 = 4.5\ fA/\sqrt{Hz}$ is equal to:

$$E_{ni} = K_4\left[1 + \frac{R_f}{R_s}\right]\sqrt{f_3 - f_1}. \tag{34}$$

Next, the contribution of the resistor noise of the TIA circuit is given by:

$$E_{nR} = \sqrt{4k_BTR_fBW}. \tag{35}$$

Optics EXPRESS

The total noise at the output of TIA is given by:

$$E_{ntotal} = \sqrt{E_{np}^2 + E_{n1}^2 + E_{n2}^2 + E_{n3}^2 + E_{ni}^2 + E_{nR}^2}. \tag{36}$$

Finally, after the differentiation of two diodes and the remaining gain of the circuit the RMS noise can be estimated for the complete circuit

$$E_{nout} = G_{OPA}\sqrt{2(E_{ntotal})^2}. \tag{37}$$

In Table 5 we summarize the different noise contributions.

The analytical estimate for the total output noise with no incident light at the split-detector ($I_p = 0$) is $E_{nout}^{ab} = 8.34\ mV_{RMS}$ which roughly agrees with the experimental values $E_{out}^{eb} = 7.8\ mV_{RMS}$, measured with a RMS voltmeter R&S URE3. Further, the estimate of the noise with the detector unblocked and no laser light is $E_{nout}^{e} = 14\ mV_{RMS}$. The increased level is due to ambient noise that is not considered in the analytical model.

Table 5. The noise budget of the detector circuit in μV_{RMS}

Noise Contribution	E_{nR}	E_{n3}	E_{np}	E_{n1}	E_{n2}	E_{ni}
μV_{RMS}	11.37	1.75	0.133	0.02	0.002	2.25e-4

Appendix C

The scanning piezo stage used in the setup (P-629.2CD by Physik Instrumente) is directed mounted on an optical table, and not directly attached to the vertical breadboard containing the optical CFS elements (mounted on the pillar Fig. 1(A)). In closed-loop operation, a built-in sensor is used to monitor the position of the stage in real time. The error signal is sent to the controller to provide accurate nanopositioning. External vibrations can affect the piezo position in both horizontal and vertical directions. Based on the steady-state observation of the feedback signal, one can identify the spectral characteristics of the vibrations of the setup (Fig. 8). From the time-domain signal of the x and y - axis position (Fig. 8(A)) there is up to 25 nm displacement from the target zero position. The residual noise Fig. 8(A)) and B), is caused by the electronic itself due to the high-frequency components that the piezo actuator is not able to convert into motion. The effect of this noise is a horizontal mismatch between the peaks of the signal in consecutive scans that is estimated to be 16 nm. This could be considered as the piezo-induced limit for the particle positioning accuracy. As a comparison, in the x and y - axis position (Fig. 8(C)) there is up to 40 nm displacement from the target zero position. The cause is understood from the corresponding frequency domain representation (Fig. 8(D)) where there are spectral contributions of 43 Hz, 47 Hz, and 100 Hz. After investigation, the 43 Hz was attributed vibrations induced by the lock-in amplifier that was situated on the same optical table. Further, one of the air pressured legs from the optical table was incorrectly placed such that there was a mechanical contact between one of the legs and the table. This allowed building vibrations to pass around to the table. After removing the lock-in amplifier from the optical table and readjusting the table leg, the 43 and 47 Hz peaks disappeared (Fig. 8(B)).

Apart from the horizontal displacement of the piezo table due to vibrations, the latter could also affect the z-position of the sample with respect to the focussing objective. We can update the formalism for the pupil plane amplitude of A_s and A_p to account for the small defocusing $\delta z \ll d/2$. Defocusing is equivalent to shifting the position of a particle along the z axis by $r = Z$. Thus the correction is needed in the second term of Eqs. (9) and (10) by including the phase shift

Optics EXPRESS

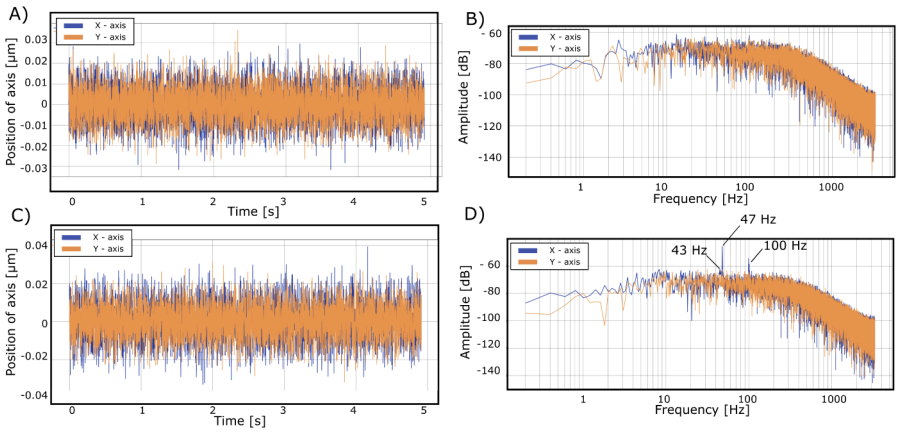

Fig. 8. The time-domain (left) and corresponding frequency domain (right) mechanical noise of the piezo stage. A) and B) showing the current state of the piezo noise . C) and D) examplify how the controller of the piezo stage compensates for the multiple sources of the vibration: 43, 47 and 100 Hz.

of ik_zZ.

$$A_s^{out} \approx r_s A_s^{inc} - (1 + r_s)\frac{\alpha}{2i\epsilon_0}\left[\frac{k^2 k_y}{k_z\sqrt{k_x^2 + k_y^2}}\right]E^f(x)e^{ik_xX}e^{ik_zZ} \tag{38}$$

$$A_p^{out} \approx r_p A_p^{inc} + (1 + r_p)\frac{\alpha}{2i\epsilon_0}\left[\frac{kk_x}{\sqrt{k_x^2 + k_y^2}}\right]E^f(x)e^{ik_xX}e^{ik_zZ}. \tag{39}$$

The effect of a slight defocus on the simulated LR profile is demonstrated in Fig. 9 We can give an estimate that on average the V_{pp} drops by 0.7% per one nanometer of defocus. Further,

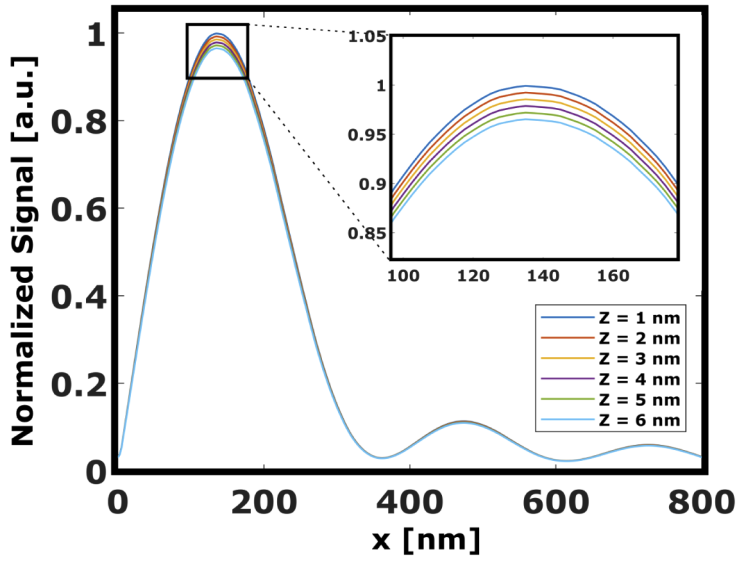

Fig. 9. Normalized simulated signal of the LR profile based on a single dipole model. Scan line along the x-direction combined with a z-defocus of one nanometer per profile.

Optics EXPRESS

the possible z-displacement can be computed as $\Delta z = \sigma(V_{pp})/(c_z \overline{V}_{pp})$. For the observed 60 nm PSL on silicon sample signal, amplitude fluctuation renders the defocus of $\Delta z' = 4.7$ nm which has been reduced to $\Delta z = 3$ nm when the remaining fluctuation due to vibration sources were removed.

Funding. Stichting voor de Technische Wetenschappen (14660).

Acknowledgments. We gratefully acknowledge the help provided by TNO in the fabrication and AFM analysis of samples. D.K. and I.E.Z. acknowledge the High Tech Systems and Materials Research Program with Project n. 14660, financed by the Netherlands Organisation for Scientific Research (NWO), Applied and Technical Sciences division (TTW) for funding this research. The authors thank Prof. H.P. Urbach for helpful assistance and discussions. The authors acknowledge numerical simulation support from M. Hammerschmidt from JCMwave.

Disclosures. The authors declare no conflicts of interest.

References

1. K. Luke, P. Kharel, C. Reimer, L. He, M. Loncar, and M. Zhang, "Wafer-scale low-loss lithium niobate photonic integrated circuits," Opt. Express **28**(17), 24452–24458 (2020).
2. J. Wang, F. Sciarrino, A. Laing, and M. G. Thompson, "Integrated photonic quantum technologies," Nat. Photonics , 1–12 (2019).
3. Z. Cheng, C. Ríos, W. H. Pernice, C. D. Wright, and H. Bhaskaran, "On-chip photonic synapse," Sci. Adv. **3**(9), e1700160 (2017).
4. K. Xu, Y. Chen, T. A. Okhai, and L. W. Snyman, "Micro optical sensors based on avalanching silicon light-emitting devices monolithically integrated on chips," Opt. Mater. Express **9**(10), 3985–3997 (2019).
5. Y. Ji, H. Wang, J. Cui, M. Yu, Z. Yang, and L. Bai, "All-optical signal processing technologies in flexible optical networks," Photonic Netw. Commun. **38**(1), 14–36 (2019).
6. A. Alfalou and C. Brosseau, *Chapter two - recent advances in optical image processing* (Elsevier, 2015), pp. 119–262.
7. J. Zhu, Y. Liu, X. Yu, R. Zhou, J.-M. Jin, and L. L. Goddard, "Sensing sub-10 nm wide perturbations in background nanopatterns using optical pseudoelectrodynamics microscopy (opem)," Nano Lett. **19**(8), 5347–5355 (2019).
8. G. E. Moore, "Cramming more components onto integrated circuits, reprinted from electronics, volume 38, number 8, april 19, 1965, pp.114 ff," IEEE Solid-State Circuits Soc. Newsl. **11**(3), 33–35 (2006).
9. K. Flamm, "Measuring moore's law: evidence from price, cost, and quality indexes, national biuro of economic research," Tech. rep., Working Paper (2018).
10. E. Barouch and S. L. Knodle, "Scatterometry as a practical in-situ metrology technology," in *Metrology, Inspection, and Process Control for Microlithography XVII*, vol. 5038 (International Society for Optics and Photonics, 2003), pp. 559–567.
11. N. Kumar, O. El Gawhary, S. Roy, V. Kutchoukov, S. Pereira, W. Coene, and H. Urbach, "Coherent fourier scatterometry: tool for improved sensitivity in semiconductor metrology," in *Metrology, Inspection, and Process Control for Microlithography XXVI*, vol. 8324 (International Society for Optics and Photonics, 2012), p. 83240Q.
12. S. Roy, A. C. Assafrao, S. F. Pereira, and H. P. Urbach, "Coherent fourier scatterometry for detection of nanometer-sized particles on a planar substrate surface," Opt. Express **22**(11), 13250–13262 (2014).
13. D. Kolenov, R. C. Horsten, and S. F. Pereira, "Heterodyne detection system for nanoparticle detection using coherent Fourier scatterometry," in *Optical Measurement Systems for Industrial Inspection XI*, vol. 11056 P. Lehmann, W. Osten, and A. A. G. Jr, eds., International Society for Optics and Photonics (SPIE, 2019), pp. 336–342.
14. D. Kolenov, P. Meng, and S. Pereira, "A highly sensitive laser focus positioning method with sub-micrometre accuracy using coherent fourier scatterometry," Meas. Sci. Technol. **31**(6), 064007 (2020).
15. D. Kolenov and S. F. Pereira, "Machine learning techniques applied for the detection of nanoparticles on surfaces using coherent fourier scatterometry," Opt. Express **28**(13), 19163–19186 (2020).
16. D. Kolenov, D. Davidse, J. Le Cam, and S. Pereira, "Convolutional neural network applied for nanoparticle classification using coherent scaterometry data," in *EPJ Web of Conferences*, vol. 238 (EDP Sciences, 2020), p. 06017.
17. A. T. Young, "Rayleigh scattering," Appl. Opt. **20**(4), 533–535 (1981).
18. X. Wei, A. J. Wachters, and H. P. Urbach, "Finite-element model for three-dimensional optical scattering problems," J. Opt. Soc. Am. A **24**(3), 866–881 (2007).
19. S. Roy, K. Ushakova, Q. Van den Berg, S. Pereira, and H. Urbach, "Radially polarized light for detection and nanolocalization of dielectric particles on a planar substrate," Phys. Rev. Lett. **114**(10), 103903 (2015).
20. R. Dorn, S. Quabis, and G. Leuchs, "The focus of light - linear polarization breaks the rotational symmetry of the focal spot," J. Mod. Opt. 50, (2003).
21. V. Ignatowsky, "Diffraction by a lens of arbitrary aperture," Trans. Opt. Inst **1**, 1–36 (1919).
22. B. Richards and E. Wolf, "Electromagnetic diffraction in optical systems, ii. structure of the image field in an aplanatic system," Proc. Royal Soc. London. Ser. A. Math. Phys. Sci. **253**(1274), 358–379 (1959).
23. A. Costa Assafrao, "On super resolved spots in the near-field regime," PhD dissertation, TU Delft (2013).
24. M. Neugebauer, P. Woźniak, A. Bag, G. Leuchs, and P. Banzer, "Polarization-controlled directional scattering for nanoscopic position sensing," Nat. Commun. **7**(1), 11286–6 (2016).

Optics EXPRESS

25. V. P. Maltsev and K. A. Semyanov, *Characterisation of bio-particles from light scattering* (Walter de Gruyter, 2013), pp. 35–117.
26. E. W. Howard, R. Huff Randal, and K. Goodall, "Measurement of Silicon Particles by Laser Surface Scanning and Angle-Resolved Light Scattering," J. Electrochem. Soc. **144**(1), 243–250 (2019).
27. A. Cox, A. J. DeWeerd, and J. Linden, "An experiment to measure mie and rayleigh total scattering cross sections," Am. J. Phys. **70**(6), 620–625 (2002).
28. S. Burger, L. Zschiedrich, F. Schmidt, R. Köhle, T. Henkel, B. Küchler, and C. Nölscher, "3D simulations of electromagnetic fields in nanostructures using the time-harmonic finite-element method," in *Modeling Aspects in Optical Metrology*, vol. 6617 H. Bosse, B. Bodermann, and R. M. Silver, eds., International Society for Optics and Photonics (SPIE, 2007), pp. 255–265.
29. A. A. Maradudin, *Light scattering and nanoscale surface roughness*, chap. 7 (Springer Science & Business Media, 2010), pp. 211–231.
30. B. Jean-Luc and D. Bruno, "Contamination monitoring and analysis in semiconductor manufacturing," Semicond. Technol 57–78 (1999).
31. B. Brown, "Noise analysis of fet transimpedance amplifiers," Texas Instrum. Dallas, TX, USA, Tech. Rep.[Online]. Available: http://www.ti.com/lit/an/sboa060/sboa060.pdf, (1994).